The Archives of Automotive Engineering – Archiwum Motoryzacji Vol. 110, No. 4, 2025
https://doi.org/10.14669/AM/208687

FUEL CELL SYSTEM INTEGRATION WITH DIFFERENT OXYGEN REDUCTION REACTION CATALYTIC MATERIALS IN FUEL CELL VEHICLE USING SIMULATION TOOL

SHIVAKUMAR NAGAREDDY[1], ASHOK KUMAR BABU CHELLAM[2],
SIVA SUBRAMANIAN RAJESWARAN[3],
SANGEETH KUMAR MADHESWARAN[4], VEERAMANI NEELAKANDAN[5]

Abstract

With the increase of conventional fuels demand, increase in fuel price, battery charging restrictions in electric vehicles during long travel and costlier technologies to implement the current (or) future emission regulations, the hydrogen fuelled fuel cell system plays an important role. In recent fuel cell system, the platinum catalyst material is used for oxygen reduction reaction (ORR) which is costlier. The main aim of this research work is to find the low priced and better (or) highly performing oxygen reduction reaction catalyst materials in proton exchange membrane fuel cells. In this study, AMESim simulation tool was used to analyse the fuel cell system with different catalyst materials such as platinum, $Fe–N_2–C$ and Ag–alloy (Ag–Cu) for better oxygen oxidation reaction under dynamic conditions using adaptive Jacobian computation method. From the simulation results, the performance of catalyst materials used in the fuel cell system were compared with respect to vehicle performance, powertrain and stack output power, battery state of charge (SoC), compressor efficiency with air mass flow rate, hydrogen fuel efficiency and power/energy distribution.

---

[1] Mechanical Engineering, Chennai Institute of Technology, Kundrathur, 600069, Chennai, India, email: shiva.thermal1980@gmail.com, ORCID: 0000-0001-9084-9101

[2] Mechanical Engineering, Nandha Engineering College, 638052, Erode, India, email: ashokbkumar@yahoo.com, ORCID: 0000-0002-9291-1797

[3] Mechanical Engineering, Sir Krishna College of Engineering and Technology, 641008, Coimbatore, India, email: sivasugiri@gmail.com, ORCID: 0000-0001-6137-1567

[4] Mechanical Engineering, Sona College of Technology, 636005, Salem, India, email: sangeet13@gmail.com, ORCID: 0000-0001-8765-5074

[5] Electrical and Electronics Engineering Department, Sri Krishna College of Engineering, 631003, Arakkonam, India, email: mailtoveeramani@yahoo.co.in, ORCID: 0009-0001-4853-7662

The fuel cell system with Fe–N_2–C catalyst material shows nearly the same overall system performance when compare with platinum catalyst material, but the fuel cell system with Al-alloy shows comparatively less overall system performance than platinum and Fe–N_2–C catalyst materials used in the fuel cell system. Also, the price of platinum is much expensive than Fe–N_2–C material which makes the system costlier. From the simulation results comparison, the fuel cell system with Fe–N_2–C catalyst proves better overall performance and cost benefited than Platinum and Ag-alloy catalyst materials.

Keywords: hydrogen fuel cell; oxygen reduction reaction; fuel cell Simulation; Fe–N–C catalyst; Ag-alloy catalyst

1. Introduction

The existing proton exchange membrane fuel cell system was using platinum catalyst for oxygen reduction reaction. The system makes costly because of costlier catalyst material used in the stack to optimize the overall performance of the system. To reduce the cost of the system as well as to operate the system with nearly same (or) better performance than the existing catalyst, there is a demand for the materials which suit the similar materials properties such as exchange current density and activation energy for oxygen reduction reaction.

1.1. Bibliography Analysis

The performance analysis of proton exchange membrane (PEM) fuel cell system with different cost benefit and sustainable materials with effective design and manufacturing techniques of membrane exchange assembly towards enhanced efficiency is essential. The electrolyser cell with PEM membrane was used to generate the hydrogen gas and metal hybrid storage tanks were used to store the hydrogen gas. The PEM fuel cell was used to generate an electricity and integrated with various cars [1].

Platinum based catalysts for oxygen reduction reaction provides better performance under acidic and alkaline high temperature operating conditions. The Fe–N–C (platinum group free) catalyst very effective in alkaline (improved oxygen reduction reaction performance), reduces risk of cost and chances of poisoning with phosphate electrolyte [2, 3].

The performance of high temperature PEM fuel cell depends on the penetration of acid (or) electrolyte solution through the catalyst layer. The polytetrafluorethylene (PTFE) was used to increase the strength of acid penetration and its performance was tested at different concentrations from 10% to 50% of weight. The power density of the catalyst material was increased by 34% when the PTFE increased up to 50% of weight but the porosity reduced.

The addition of 20% weight of PTFE provides better acid rejection and enhancing performance [4].

The membrane exchange assembly (MEA) is the middle part of the PEM fuel cell where the proton exchange membrane was packed with catalyst layer and gas diffusion layer on either side. The system is subjected to degradation in long cyclic load operating conditions. The PEM fuel cell models ranging from nano to macro sized were considered for better kind of degradation mechanisms in the fuel cell [5].

The reduction of platinum concentration (or) replacement of platinum catalyst is the most important phenomenon because of it gets poisoning when reacts with phosphate content in the electrolyte in case of high temperature PEM fuel cells and also due to being expensive in nature. The Fe-N-C catalyst replaces 25% of platinum nickel-alloy catalyst by maintaining better oxygen reduction reaction performance with cost benefit. This hybrid membrane exchange assembly increases cell voltage continuously over an operating time and performs prolonged activation. Also, this hybrid MEA improves mass transport and no chances of harmful “by products” at high temperature PEM fuel cell operation [6].

A hybrid electrocatalyst was utilized in PEM fuel cell system which comprise of automatically dispersed platinum and Fe single atoms, and Pt-Fe alloy nono-particles. The mass activity of this hybrid electrocatalyst was shown 3.8 times greater than Platinum-C catalyst. A very lesser platinum mass of 0.015 mg/cm^2 loading in the cathode results in exceptional stability and no responsible current collapse at 0.6V for more than 200 hours [7]. The hybrid Pt/Fe-N-C catalyst with 1% to 2% wt of platinum shows the same current density of 0.8 V like Fe-N-C catalyst but the hybrid one is more stable during its operation [8].

From the reviewed platinum group free Fe-N-C based catalysts, $Fe-N_2$ catalyst has most active sites for oxygen reduction reaction as per their structural characterisation. $Fe-N_4$ catalyst shows next to $Fe-N_2$ catalyst with respect to activity due to enhanced oxygen binding and electron transport. [9]. Fe-N-C catalysts provide $4e^-$ pathway in case of alkaline operating conditions.

The alternative Fe-N-C catalysts show lower activation energy which is essential for better ORR in PEM fuel cells to replace high-priced platinum based catalysts. The Fe-N-C catalysts must avoid Fe based nano-particles to reduce poisoning of membrane and also to reduce the fuel cell performance. Also, these alternative catalyst materials must have high graphitization and low edge defect density to reduce the chance of corrosion and improve the fuel cell system durability [10, 11].

To improve the activity and stability of catalyst materials used in fuel cell for ORR in acidic medium, platinum group metal free catalysts such as Fe-Sn-N-C were used with different Fe-Sn ratios using metal organic framework based approach. The more concentrations of pyridine and pyrolic nitrogen results in enhanced ORR activity. Fe-Sn-N-C catalysts yield less H_2O_2 which results in better selectivity towards $4e^-$ ORR pathway and improved durability [12].

The platinum group metal free Fe-N-C catalyst extracted from nitrogen (or) sulphur doped synthetic polymers show better performing cathode catalyst layer which provides peak power density of around 0.15 W/cm^2 in PEM fuel cell. Sulphur doped Fe-N-C catalyst produces lower H_2O_2 by-product with $4e^-$ ORR [13].

The oxygen doping in Fe-N_4 species would enhance the electronic structure and binding between O-Fe-N_4-C-O and hydroxide group, it leads to boost up the oxygen reduction reaction performance. The power density of O-Fe-N_4-C-O species PEM fuel cell was about 0.88 W/cm^2 which is around 16% and 31% higher than O-Fe-N_4-C and Fe-N_4-C species PEM fuel cells [14].

The Fe-N-C catalysts show effective performance on oxygen reduction reaction but its weekend stability/durability seriously limits its commercial utilization. The review elaborates the relation between the active centres and stability of Fe-N-C catalysts. Fe-N_x-C_y and Fe_2-N_x-C_y were show excellent steadiness of activity and stability [15].

Using nitrite, nitric oxide and hydroxylamine probes, the ORR of the catalyst Fe-N-C was improved under both acidic and alkaline operating conditions. The study concludes, the catalyst was highly active with nitride and nitric oxide electro-reduction at different pH values where ammonia as by-product [16].

Different binary and ternary Ag nono-alloys such as Ag-Cu, Ag-Pd, Ag-Au, Ag-Co etc. were used as effective platinum free electro-catalysts for oxygen reduction reaction in PEM alkaline fuel cells. The Ag-Cu electro-catalyst produces a cell voltage of 0.81 V, and Ag-Au and Ag-Pd electro-catalysts produce a cell voltage from 0.86 V to 0.90 V [17].

The Ag based electro-catalysts where the Ag particles electro-deposited with nitrogen doped grapheme oxide, graphene, multi-walled carbon nano-tube were analysed for ORR activity. The electro-deposited Ag catalysts allow four electron pathway in alkaline medium and these catalyst materials confirm alternative for platinum based catalyst to be utilized in alkaline medium PEM fuel cells [18]. The Au-Ag nano-alloy catalyst tracks a $4e^-$ ORR pathway which is validated and demonstrated that the system projects a maximum power density of 98.2 mW/cm^2 at current density of 444 mA/cm^2 in each hydrogen fuel cell [19]. Ag/C, Cu/C and bimetallic Ag and Cu with carbon were used as catalysts for the ORR in an anion exchange membrane fuel cell. The bimetallic catalyst provides a higher power density than single metallic catalysts due to synergistic cause between Ag and Cu particles [20].

The hybrid parallel architecture in a vehicle where it powers through fuel cell power and battery plays emerged role to satisfy power demand of a vehicle. The fuel cell system serves as a green energy source which reduces the power demand up to 40.3% and it maximum power output of 257.8 W [21].

The platinum catalyst based PEM fuel cell system was simulated using AMESim tool to summarize the hydrogen consumption, stack cooling system and stack power output over cycle duration of 3500 seconds under dynamic conditions [22]. There were opportunities for the researchers to study the PEM fuel cell system integrated with the vehicle with different catalyst materials for better oxygen reduction reaction with cost effective value [23].

To meet the future global emission standards, hydrogen fuel cell technology is the one ultimately clean energy, especially in case of commercial vehicles. The development of fuel cell system was reviewed with vehicle integration including control technologies [24]. But no alternative replacement of costlier platinum based catalyst in PEM fuel cell was involved in this study.

The AMESim simulation tool was used to analyse the performance of the PEM based fuel cell system with liquid hydrogen cold energy utilization. The cold energy of liquid hydrogen was used for cool the air entering the compressor and the coolant and the cold energy consumption ratio was maintained above 80%, except at very low temperatures and low fuel cell stack (FCS) load. The maximum 15% of energy was saved with cold energy utilization form liquid hydrogen when compare with without cold energy usage from liquid hydrogen. Also, the size of the intercooler was reduced with the reduction of intercooler heat load [25].

From the literature survey, there are many reviews on catalyst materials for oxygen reduction reaction towards replacing platinum catalyst which is costlier. But no simulation (or) experimental comparative studies on different catalyst materials for oxygen reduction reaction used in fuel cell system integrated in a vehicle with overall control strategy. In this simulation study, overall performance of Fuel Cell system integrated with a vehicle was analysed with the inclusion Platinum, $Fe-N_2-C$ and Ag-Alloy (Ag-Cu) catalyst materials, and each sub-system control. The main intension of this study is to replace the costlier platinum catalyst with cheapest one, abundantly available in earth and also which must produce nearly the same performance as platinum. Figure 1 shows the work flow chart for the simulation study on PEM fuel cell system integrated with the vehicle.

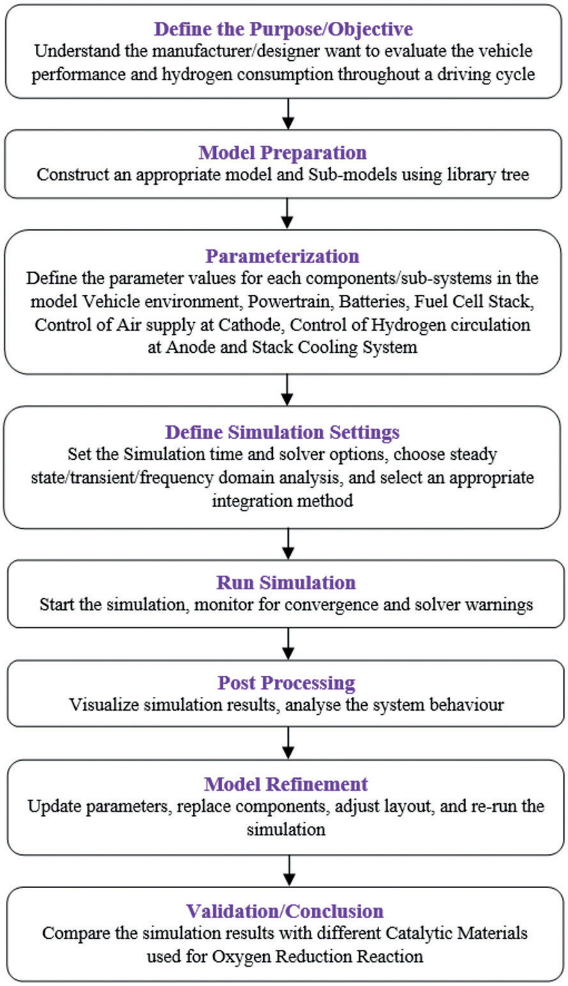

Fig. 1. Work flow chart for simulation study

2. Simulation Study

Using Library tree in AMESim simulation tool was used to model the complete PEM fuel cell system integrated with a vehicle including various control systems. The sub-systems such as gas mixture, materials and cooling system were defined in the global parameters window. Figure 2 shows the model of PEM fuel cell system with vehicle integration. The initial conditions were defined at dynamic conditions during a cycle shown in the Table 1.

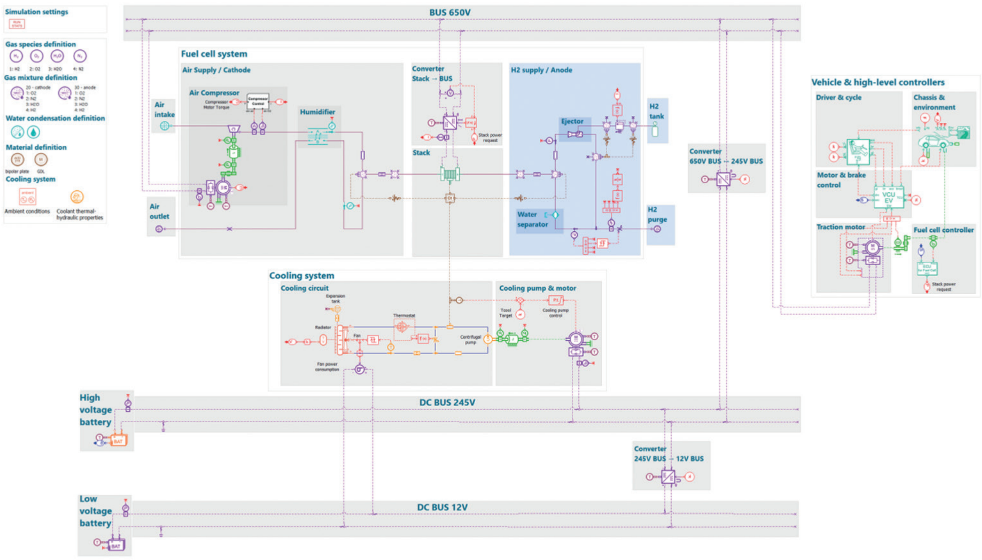

Fig. 2. Model of PEM fuel cell system with vehicle environment

Tab. 1. Initial conditions

Parameters	Values
Coolant inlet temperature, [°C]	70
Gas mixture temperature at cathode side, [°C]	70
Gas mixture temperature at anode side, [°C]	70
Gas mixture pressure at anode side, [bar]	1.5
Gas mixture pressure at cathode side, [bar]	1.0132

Before start of the simulation, operating conditions of the sub-systems were needed to be defined at the global parameters set up window. Table 2 shows the various operating parameters of the PEM fuel cell system defined. In PEM fuel cells, the stoichiometry at both anode and cathode is maintained constant and is equal to 2. At anode, each hydrogen molecule is oxidised and produces 2-electrons and 2-protons. At cathode, the reaction requires 2-protons and 2-electrons to reduce each molecule of oxygen. The constant stoichiometry at both cathode and anode leads to stable and efficient operation of fuel cell. The unbalanced stoichiometry at both anode and cathode leads to cell polarity reversal which results in damage of the fuel cell. The H_2O fraction according to humidity set for the inlet gas mixture at anode side was defined as zero and the H_2O fraction at the cathode side was calculated shown in Eq. (1).

Tab. 2. Operating parameters/conditions

Parameters	Values
Stack Pressure, [bar]	1.5
Stack Temperature, [°C]	75
Ambient Temperature, [°C]	25
Ambient Pressure, [bar]	1.0132
Ambient Relative Humidity, [%]	40
Relative Humidity (RH) at Cathode, [%]	40
O_2 Stoichiometry	2
H_2 Stoichiometry	2
Cathode O_2 fraction	0.21
Cathode N_2 fraction	0.79
Cathode H_2 fraction	0
Anode O_2 fraction	0
Anode N_2 fraction	0
Anode H_2 fraction	1
Anode H_2O fraction according to humidity set for the inlet gas mixture at anode side	0

Cathode H_2O fraction according to humidity set for the inlet gas mixture at cathode side

$$= \frac{RH\ at\ cathode\ \times Water\ Saturated\ Pressure\ at\ Mixture\ Temperature\_cathode}{100\ \times Stack\ Pressure\ \times 10^5} \tag{1}$$

2.1. Vehicle Characteristics and Controllers

The PEM fuel cell system was integrated with the vehicle including various control systems. The vehicle/car specifications such as gross vehicle weight, gear ratio, maximum powertrain torque, radiator to vehicle speed ratio and coolant fan nominal power were chosen for the simulation study and defined in the global parameters set up. Table 3 shows the required vehicle specifications for the simulation study.

Tab. 3. Vehicle specifications for the simulation study

Parameters	Values
Total vehicle mass, [kg]	1690
Gear ratio	5
Maximum brake torque, [Nm]	215
Radiator to vehicle speed ratio	0.125
Fan nominal power, [W]	200

2.2. Battery and Electric Network

The 650 V developed power from the FCS was utilized to operate the air compressor and the powertrain/traction motor to drive the vehicle. A 650 V power was converted into 245 V using BUS converter was utilized to operate FCS cooling system's coolant pump and to store it in the respective capacity battery. Later, a 245 V power was converted into 12 V to operate fuel cell system cooling circuit, and to store it in the respective capacity battery which is required to handle the various electrical devices in the vehicle environment. The electrical network connections were made as per the control system strategy.

The FCS produces the stack output voltage which depends on the current intensity of the catalyst material used in the FCS, the temperature and operating parameters defined at the anode and cathode side of the stack. Table 4 shows the different FCS geometry parameter values defined in the global parameters window.

Tab. 4. Fuel cell stack geometry

Parameters	Values
Number of cells in series (N_cell)	370
Cell active area (A_cell), [cm^2]	237
Gas Mixture Side:	
Number of parallel channels in the bipolar at cathode side	24
Number of parallel channels in the bipolar at cathode side	3
Channel height at cathode side, [mm]	1
Channel height at anode side, [mm]	1
Channel width at the cathode side (w_c), [mm]	1
Channel width at the anode side (w_a), [mm]	1
Landing to channel width at cathode side, [mm]	w_c
Landing to channel width at anode side, [mm]	w_a
Cooling Side:	
Cell Length to Width ratio (LWratio)	4/3
Cooling channel width (W_cooling), [mm]	2
Cooling channel landing width (W_cooling_land), [mm]	3
Cooling channel height (h_cooling), [mm]	1
Thermostat low temperature, [°C]	70
Thermostat high temperature, [°C]	78
GDL Characteristics:	
Permeability at the cathode side, [m^2]	1*10-14
Permeability at the anode side, [m^2]	1*10-14
Porosity at cathode side	0.82
Porosity at anode side	0.82
Thickness at cathode side, [mm]	0.2

Tab. 4. Fuel cell stack geometry; cd.

Parameters	Values
Thickness at anode side, [mm]	0.2
O_2 alteration co-efficient at GDL cathode	0.05
Membrane Electrode Assembly Properties:	
Cathode catalyst loading, [mg Ag/cm^2]	0.3
Catalyst specific area, [cm^2 Ag/mg Ag]	800
Reference exchange current density, [mA/cm^2 Ag]	1*10–5
Membrane Proton Resistance, [ohm.cm^2]	0.147
Catalyst Layer thickness at cathode, [mm]	0.015
Catalyst Layer thickness at anode, [mm]	0.015
Exchange current density reference temperature, [K]	25+273.15
Activation energy for O_2 reduction on Silver, [J/mol]	15600
Faraday constant	96485.34

Channel length at cathode side,

$$= (A\_cell \times 100)/((Channel\ Width + Landing\ to\ channel\ Width\ at\ cathode) \times Number\ of\ parallel\ channels\ in\ the\ bipolar\ plate\ at\ cathode) \tag{2}$$

Channel length at Anode side,

$$= (A\_cell \times 100)/((Channel\ Width + Landing\ to\ channel\ Width\ at\ anode) \times Number\ of\ parallel\ channels\ in\ the\ bipolar\ plate\ at\ anode) \tag{3}$$

Cell Length, $$L\_cell = \sqrt{A_{cell} \times LWratio \times 100} \tag{4}$$

Cell Width, $$W\_cell = \frac{L\_cell}{LWratio} \tag{5}$$

Number of parallel channels cooling side,

$$N\_channels\_cooling = \frac{Floor(0.8 \times W\_cell)}{W\_cooling + W\_cooling\_land} \tag{6}$$

Total sectional area of cooling channel,

$$A\_cooling\_channel = W\_cooling \times h\_cooling \times N\_channels\_cooling \times N\_cell \tag{7}$$

Cooling channel wet perimeter,

$$P\_cooling\_channel = 2(W\_cooling + h\_cooling) \times N\_channels\_cooling \times N\_cell \tag{8}$$

Cooling channel hydraulic diameter,

$$Dh\_cooling\_channel = \frac{4 \times A\_coling\_channel}{P\_cooling\_channel} \tag{9}$$

Tab. 5. Stack DCDC converter power supply details

Parameters	Values
Minimum stack current density (I_stack_min), [mA/cm^2]	20
Maximum stack current density (I_stack_max), [mA/cm^2]	2000
Fuel cell stack DCDC efficiency	0.95
High voltage, [V]	650

Table 5 shows the stack DCDC converter power supply details. The minimum and maximum stack DCDC output current density can be calculated using the equations:

$$I\_\min\ \_DCDC\_out = \frac{stack\ DCDC\ Eff.(I\_stack\_\min \times A\_cell)}{1000} \times \frac{\mathrm{Vin}}{Vout} \tag{10}$$

and

$$I\_\max\ \_DCDC\_out = \frac{stack\ DCDC\ Eff.(I\_stack\_\max \times A\_cell)}{1000} \times \frac{\mathrm{Vin}}{Vout} \tag{11}$$

2.4. Air Flow Control at Cathode Side

The PEM fuel cell system uses centrifugal compressor to supply the mass flow of air to the stack at the cathode side. The electric motor demands torque required to drive the compressor to ensure the stoichiometry target of oxygen. The speed reduction ratio was applied between the motor and the compressor. The pressure ratio and isentropic efficiency of the centrifugal compressor depends on the corrected compressor rotary velocity and the corrected mass flow rate of air entering the stack. Humidifier was used to dry the compressed air into wet air before entering the stack. There were two gas mixture chambers used and separated by a diffusion component just before the stack.

2.5. Hydrogen Supply Loop at Anode Side

The hydrogen gas at 700 bar from the storage tank was used to supply to the anode through pressure regulator. Table 6 shows the hydrogen storage parameter values maintained at the anode side of the fuel cell. Elector was used to ensure the recirculation of hydrogen gas through anode. There were two gas mixture chambers used and separated by a diffusion component just before the stack. A water separator which removes out the liquid water from anode side of the stack. A purge valve is opened when the molar fraction of the nitrogen reaches higher than the target range, but is loses some mass of hydrogen while removing unwanted inert gases and water to overcome the stack performance drop.

Tab. 6. Hydrogen storage parameter values

Parameters	Values
Hydrogen storage pressure, [bar]	700
Hydrogen mass storage capacity, [kg]	5
Hydrogen storage temperature, [°C]	25
Hydrogen molar mass, [kg/mol]	2.01588/1000
Latent heat of hydrogen, [kJ/kg]	119.93

Hydrogen tank volume can be calculated from the relation:

$$PV = n\,RT = \frac{m}{M}\,RT \tag{12}$$

where n = (m/M) is number of moles, m is the mass of hydrogen gas in kg, M is the molar mass in kg/mol, R is the universal gas constant = 8.314 J/mol. K, and T is the temperature of the gas stored in K.

$$V = \frac{m}{M \times P}\,RT \quad \text{in m}^3 \tag{13}$$

2.6. Fuel Cell Stack Cooling System

The cooling system used in FCS is to control the stack temperature within the threshold limit. A coolant pump was used to circulate the coolant in the cooling flow loop to absorb heat from the stack. The thermostat allows the coolant to flow into the radiator when the coolant temperature peaks above the maximum temperature limit. A cooling fan gets trigger up when additional cooling requirement demanded form the stack controller.

2.7. Run Simulation

The activation energy and exchange current density of different catalyst materials used were strictly considered in the global parameter window before start of the simulation. The fixed regular standard integrator simulation type with 1800 seconds simulation duration was chosen for the study. Energy, Power and activity were considered as additional computations under dynamic regular standard integration simulation mode. An adaptive Jacobian computation method was used to run the simulation and the results were analysed for any model refinement if necessary and the final results were summarized.

3. Results and Discussion

The fuel cell system with different catalyst materials for oxygen reduction reaction was simulated towards vehicle performance, powertrain output, stack efficiency, air supply control system, hydrogen recirculation and it consumption efficiency, stack cooling performance, and electrical energy distribution. The simulated graphs were extracted from the study and analysed for the variations over a period of 1800 seconds driving cycle.

3.1. Performance of Vehicle

From the vehicle performance simulation results, the vehicle velocity fluctuations versus driving cycle velocity, vehicle travel range versus state of charge (SoC) of the battery, power required to move the vehicle (traction power), power output from the FCS (stack power) and batter power variations were analysed throughout the period of driving cycle.

3.1.1.Variation of Cycle Velocity and Vehicle Velocity

Figure 3 show the variation of vehicle velocity and driving cycle velocity over a time duration of five hours. The velocity of the vehicle increases and decreases frequently with respect time on different road conditions. The vehicle velocity variations over time is exactly the same with respect time, because the vehicle specifications were used for the simulation study is same irrespective of the catalyst materials used for the oxygen reduction reaction in the fuel cell system integrated with the vehicle. The maximum speed (or) velocity of the vehicle was reached during a cycle is around 115 km/hr. the vehicle velocity follows the target cycle velocity very closely, the small deviations may be due to sensor error (or) lag in the control system [24].

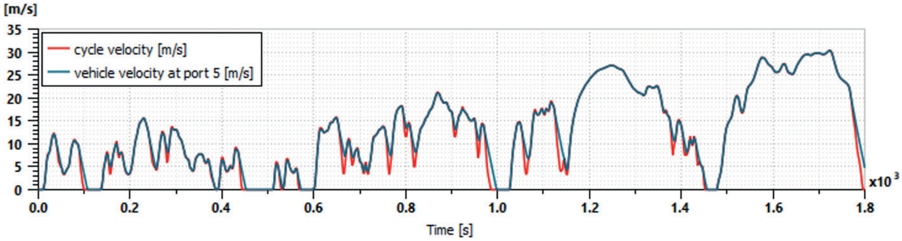

(a) For platinum catalyst material

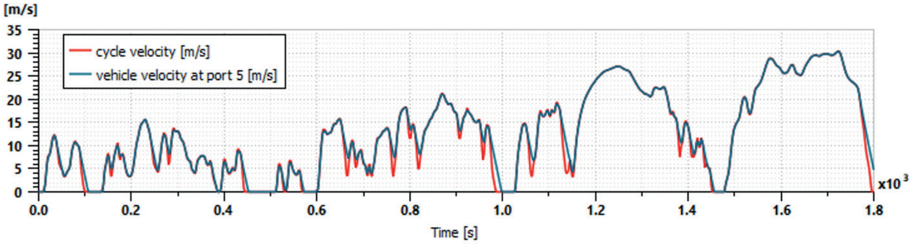

(b) For Fe-N_2-C catalyst material

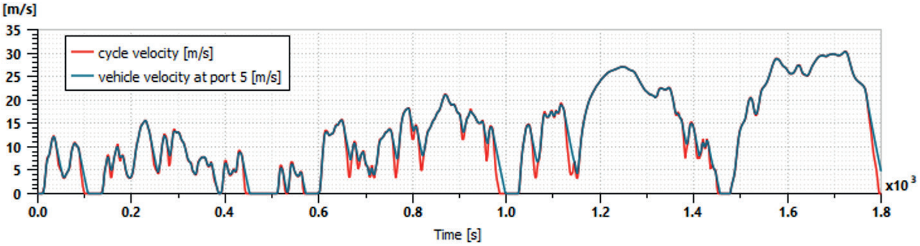

(c) For Ag-alloy catalyst material

Fig. 3. Variation of driving cycle velocity and vehicle velocity during 1800 seconds of time duration

3.1.2. Variation of Vehicle Travel Range and Battery State of Charge

The vehicle travel range is a function of state of charge of the battery and the rate of energy consumption from the battery. When SoC drops, the vehicle travel range decreases until the power consumption grow into more proficient. Figure 4 show the variation of vehicle travel range and the battery state of charge with respect to time span during a cycle of 1800 seconds. For the Catalyst materials Platinum and Fe-N_2-C, the vehicle range increases sharply at the initial stage and reached 200 km. Later the vehicle range fluctuates between 600 km to 760 km. Similarly for the catalyst material Ag-alloy, the vehicle range start at 200 km and later it fluctuates between 500 km to 660 km. The state of charge (SoC) of the battery varies between 70% to 100% for the catalyst materials Platinum and Fe-N_2-C, but for the catalyst material Ag-alloy, SoC of the battery slightly falls below 70%. The SoC of the battery starts at 100% and drops gradually over a time and ends at around 70% which shows the battery discharge from the system usage (or) driving. The increase in SoC of the battery is because of regenerative braking, recharging (or) lower energy consumption phase [22].

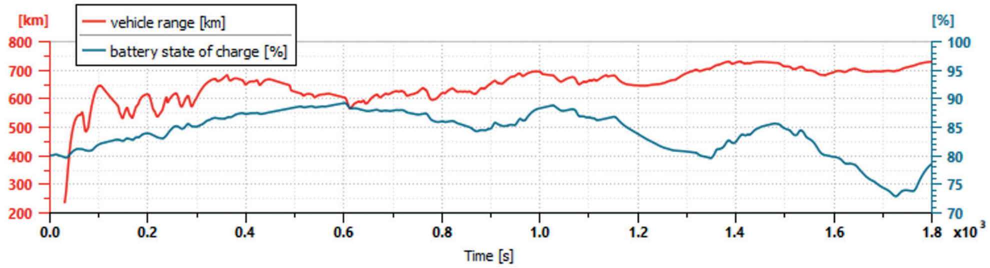

(a) For platinum catalyst material

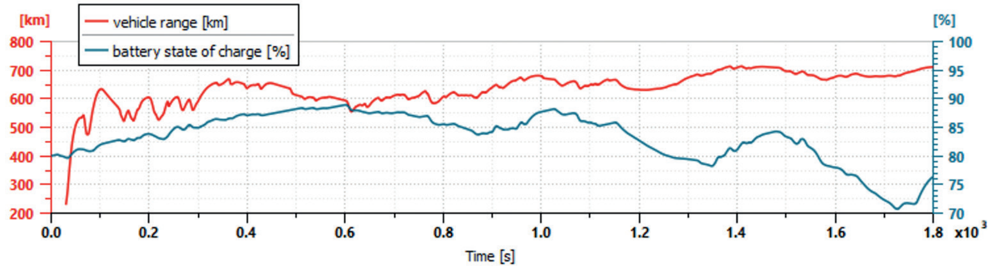

(b) For Fe-N_2-C catalyst material

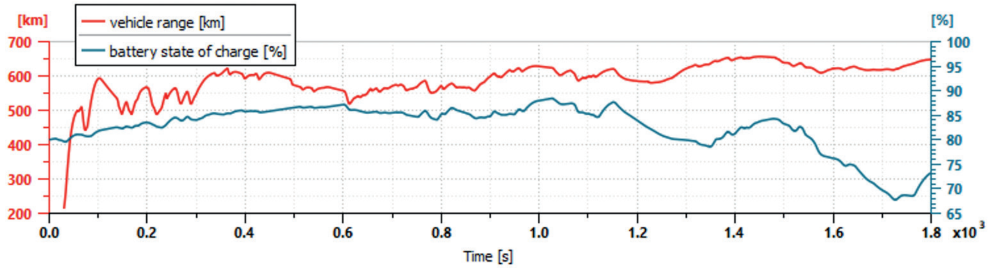

(c) For Ag-alloy catalyst material

Fig. 4. Variation of vehicle travel range and battery state of charge during 1800 seconds of time duration

3.1.3. Variation of Traction Power, Stack Power and Battery Power

Figure 5 shows the variation of traction power, stack power and batter power against 1800 seconds time duration of driving cycle. These power values range from −14 kW to 28 kW. The positive values represent the power output/traction power (power required at the wheels to move the vehicle). The negative values represent the power input because of charging (or) regenerative braking.

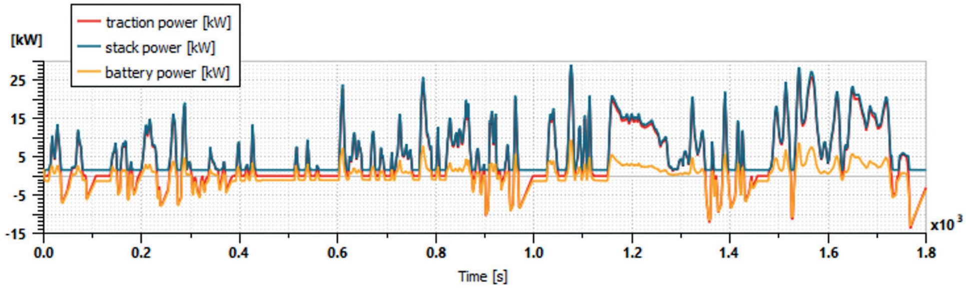

(a) For platinum catalyst material

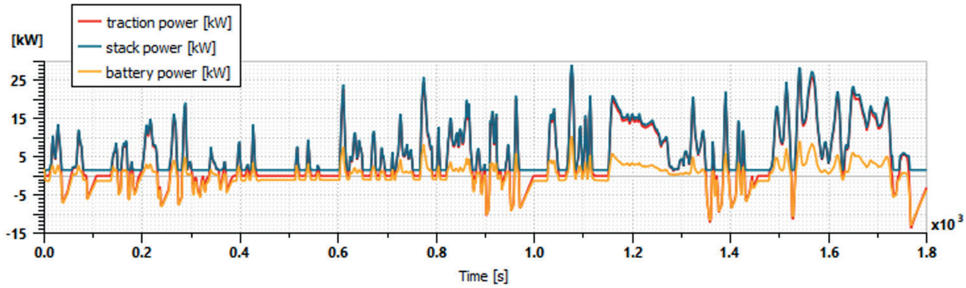

(b) For Fe–N_2–C catalyst material

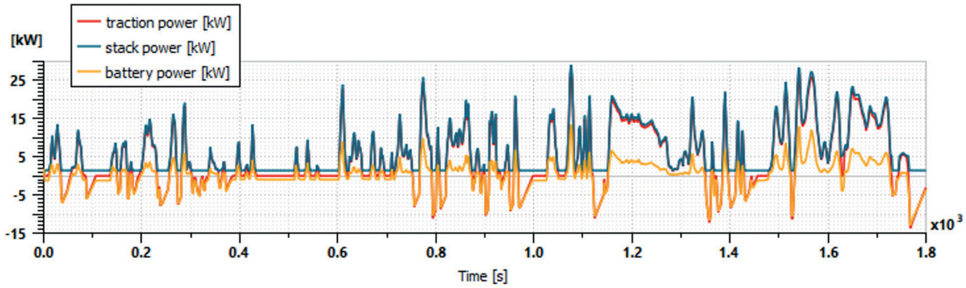

(c) For Ag–alloy catalyst material

Fig. 5. Variation of traction power, stack power and battery power during 1800 seconds of time duration

The traction power, stack power and battery power curves show the same trend for the catalyst materials platinum and Fe-N_2-C used for the oxygen reduction reaction. For Ag-alloy catalyst material, the battery power curve slightly varies between 700 seconds to 820 seconds in a driving cycle because of variation in SoC of the battery. The variation in SoC of the battery depends on exchange current density of the catalyst material used. The traction power curve represents the real time vehicle acceleration, deceleration (or) cruising, it accelerates up to 28 kW and decelerates close to –14 kW. The battery power acts like an energy barrier which supplies energy during acceleration and receives energy during deceleration (or) braking. The battery power curve below zero represents the regeneration phases where the energy is stored into the battery. The battery stores energy when the regenerative braking is in active. The stack power deliveries energy/power steadily and it contributes offload power demands from the battery during high load. Both stack power and battery power balances the energy demands (power required at the wheels to move the vehicle) to improve fuel efficiency and battery life [21, 22].

3.2. Performance of Powertrain

From the powertrain performance simulation results, the variation of torque required at the wheels to propel the vehicle verse torque demand, motor speed fluctuations as per the torque demand, motor mechanical power and its thermal loss variations, and input current verses input voltage to the motor were analysed over a period of 1800 seconds throughout a driving cycle.

3.2.1. Variation of Actual Torque and Torque Demand

The actual torque requirement from the motor output shaft is net power required at the wheels to move the vehicle. Figure 6 shows the variation of actual torque power requirement and the torque request from the vehicle control system during 1800 seconds of driving cycle.

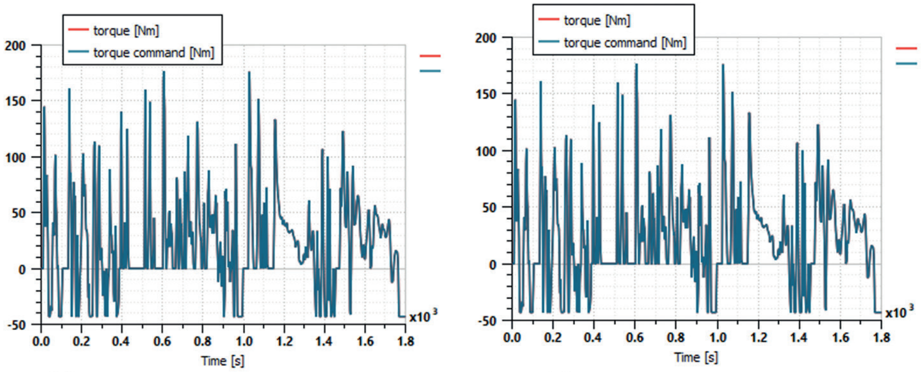

(a) For platinum catalyst material

(b) For Fe-N_2-C catalyst material

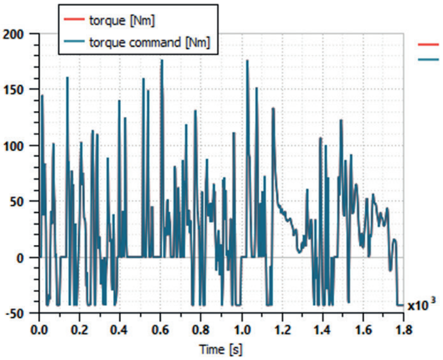

(c) For Ag-alloy catalyst material

Fig. 6. Variation of actual torque and torque request from the vehicle control system during 1800 seconds of time duration

The motor controller with control algorithm was well calibrated so that the actual torque required curve overlaps with the torque demand curve. The torque output from the motor varies between -50 Nm to 180 Nm irrespective of the catalyst materials used in fuel cell system. The variation of motor torque output depends on traction power available at the road wheels (traction power). The positive torque curve shows the acceleration mode, whereas the negative torque curve shows the deceleration (or) regenerative braking mode [21, 24].

3.2.2. Variation of Motor Mechanical Power and Motor Thermal Losses

Similar to the actual torque required at the motor shaft output, the motor mechanical power is the power output from the motor to propel the vehicle. Figure 7 shows the variation of motor mechanical power and its thermal losses over a period of 1800 seconds in driving cycle.

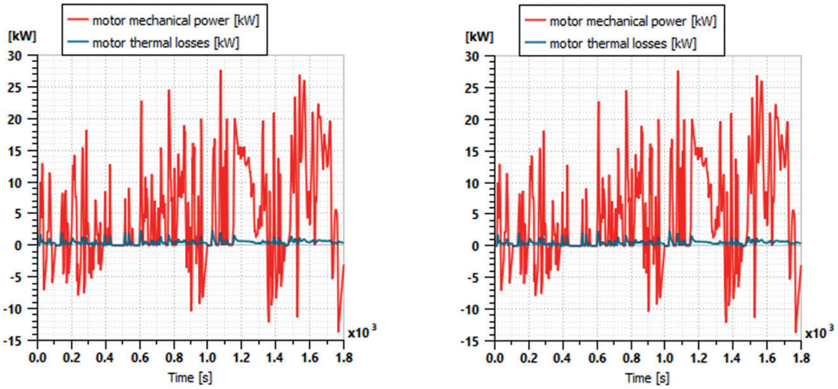

(a) For platinum catalyst material (b) For Fe–N_2–C catalyst material

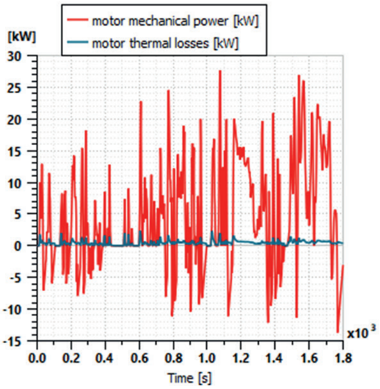

(c) For Ag-alloy catalyst material

Fig. 7. Variation of motor mechanical power and motor thermal losses during 1800 seconds of time duration

The motor mechanical power fluctuates dynamically between –14 kW to 28 kW over a cycle, the positive values show acceleration and the negative values show deceleration (or) regenerative braking. The variation trend of motor mechanical power is same as that of torque required to propel the vehicle. The motor power rises up to 28 kW during climbing (or) peak acceleration and drops below zero during regenerative braking. Because of higher resistive heating and friction generation during high load, the motor thermal losses fluctuate up to 2 kW over a driving cycle [24].

3.2.3. Variation of Motor Velocity

Figure 8 shows the variation of motor velocity (or) motor speed which actually represents how motor speed varies at different driving conditions such as acceleration, cruising, deceleration and idling over a driving cycle.

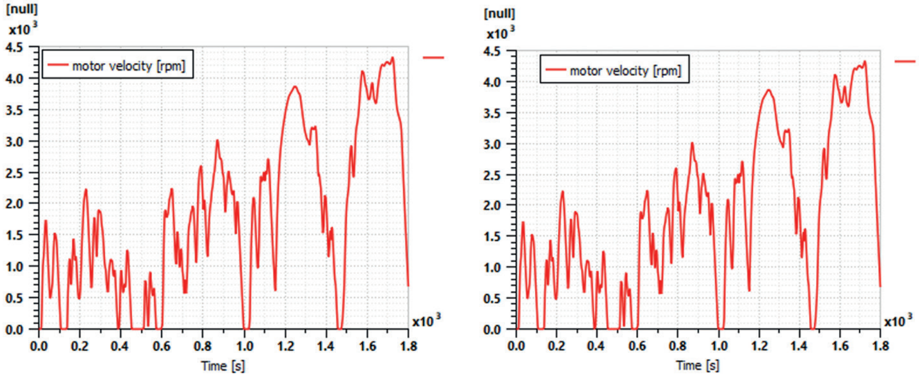

(a) For platinum catalyst material (b) For Fe-N_2-C catalyst material

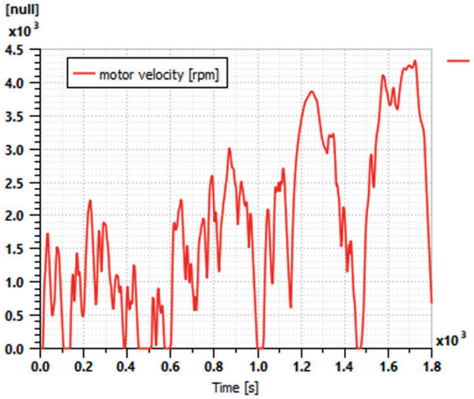

(c) For Ag-alloy catalyst material

Fig. 8. Variation of motor velocity (or) speed during 1800 seconds of time duration

The motor speed variation is exactly similar for all the catalyst materials used in fuel cell system. The motor speed increases rapidly during acceleration, it decreases during deceleration and nearly zero at idling condition. The motor speed reaches up to 4500 rpm during climbing section during a cycle. The drops in motor speed due to regenerative braking may coincide with the motor mechanical power (or) torque curves [21, 24].

3.2.4. Variation of Input Voltage and Input Current to Powertrain

Figure 9 shows the variation of input voltage and input current to a powertrain and to its controller over a period of driving cycle. The voltage from the battery was maintained around at 650 V whereas the current may fluctuate from –20 A to 45 A. The positive current values represent power received to motor and the negative current values represent the energy regaining from the regenerative braking. The variation of input voltage and input current to the motor shows exactly the trend for platinum and Fe-N_2-C catalyst materials [9], whereas it slightly varies for Ag-alloy catalyst material between 700 seconds to 820 seconds. This variation is because of similar deviations in motor torque (or) power curves due to variation in SoC of the battery [21, 24].

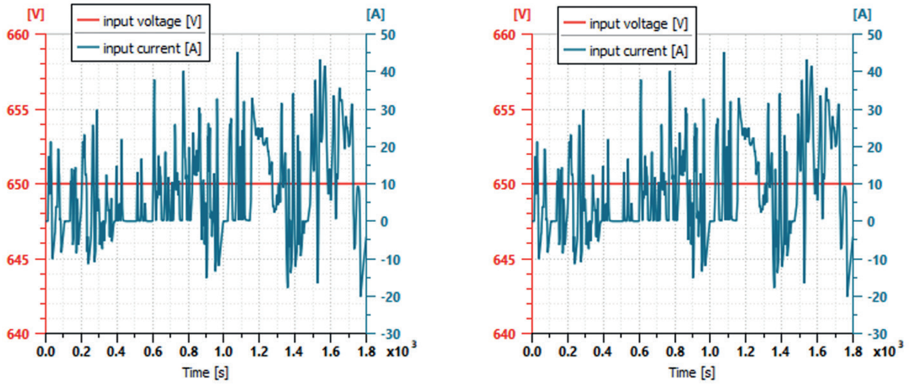

(a) For platinum catalyst material

(b) For Fe-N_2-C catalyst material

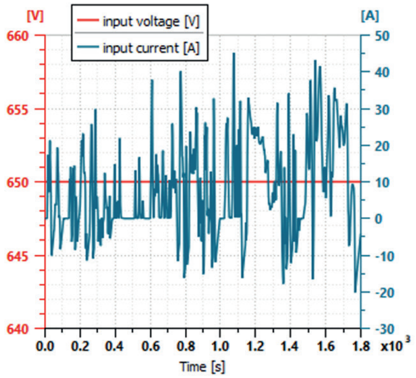

(c) For Ag-alloy catalyst material

Fig. 9. Variation of input voltage and input current to power train during 1800 seconds of time duration

3.3. Performance of Fuel Cell Stack

From the FCS performance simulation results, the fuel cell output voltage variations versus membrane exchange current density, amount of water content in the membrane versus membrane proton area resistance variations, stack power versus heat generation fluctuations within the stack, stack temperature fluctuations, coolant inlet temperature and outlet temperature variations were analysed over a period of 1800 seconds during a cycle.

3.3.1. Variation of Cell Output Voltage over Current Density

Figure 10 shows the variation of cell voltage output with respect to current density of the electrode (or) catalyst material utilized in the fuel cell for ORR. From the graph, it is clear that the cell output voltage decreases when the current density increases. The cell voltage range varies from 0.7 V to 0.93 V for the catalyst materials platinum and Fe-N_2-C, whereas 0.65 to 0.83 V for Ag-alloy catalyst material. The current density range for platinum and Fe-N_2-C catalyst materials was 0 to 450 mA/cm^2 whereas for Ag-alloy material was 0 to 520 mA/cm^2. The drop in voltage is mainly because of losses due to activation, ohmic and concentration at high current density values. Generally, the higher cell voltage output at a given current density value provides better performance of the fuel cell system [14, 17].

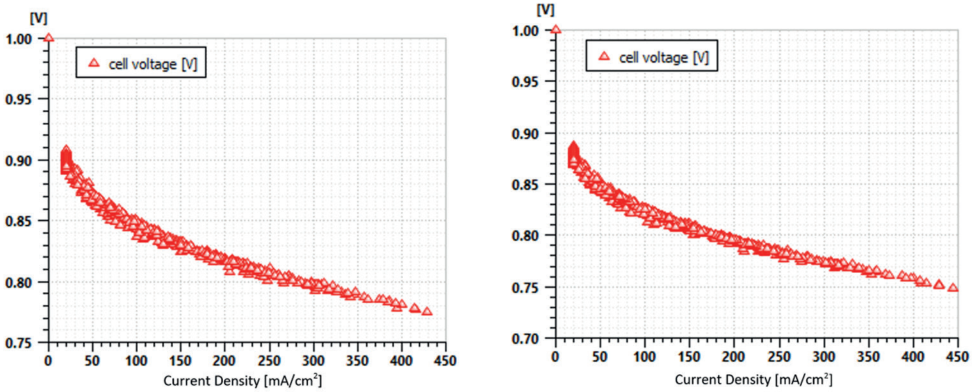

(a) For platinum catalyst material

(b) For Fe-N_2-C catalyst material

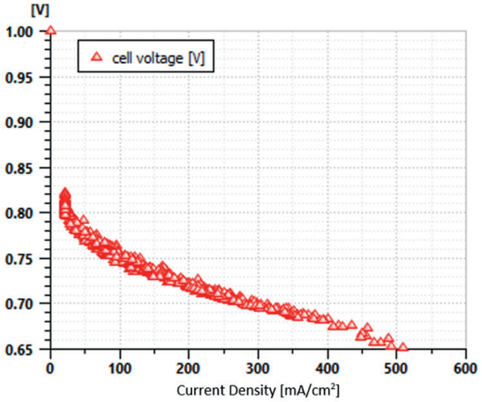

(c) For Ag-alloy catalyst material

Fig. 10. Variation of cell voltage with respect to current density during 1800 seconds of time duration

3.3.2. Variation of Actual Stack Power Output and Heat Generation from the Stack

Figure 11 shows the variation of actual stack output power and heat generation inside the stack over a period of driving cycle. The maximum stack power output was shows 30 kW for all the catalyst materials used in the fuel cell system. The heat generation from the stack for the catalyst materials platinum and Fe-N_2-C shows 20 kW. For the catalyst Ag-alloy, the heat generation shows 28 kW because higher resistive heating and frictional losses. The maximum heat generation from the stack was shows 30 kW for all the catalyst materials used in the fuel cell system. The actual stack output power lies below the maximum stack output power of 30 kW to avoid overloading (or) damage of the fuel cell components [22, 24].

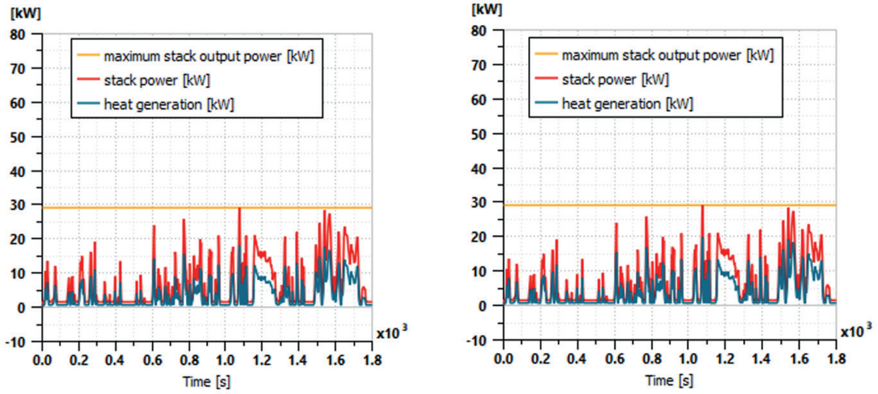

(a) For platinum catalyst material (b) For Fe-N_2-C catalyst material

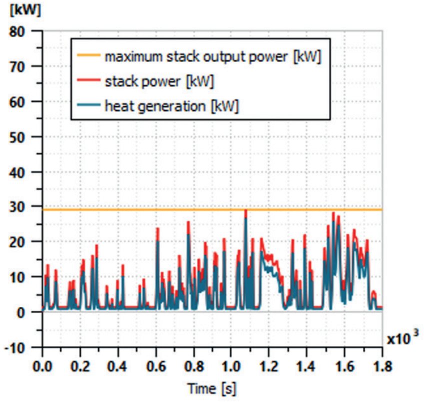

(c) For Ag-alloy catalyst material

Fig. 11. Variation of actual stack output power and heat generation inside the stack during 1800 seconds of time duration

3.3.3. Variation of Actual Stack Temperature, Coolant Inlet and Outlet Temperatures

Figure 12 shows the variation of actual stack temperature, coolant inlet and outlet temperatures, and maximum acceptable stack temperature over a driving cycle. The fuel cell coolant inlet temperature fluctuates between 70°C to 76°C below the coolant exit temperature. The fuel cell coolant outlet temperature fluctuates between 76°C to 80°C below the maximum safe operating stack temperature. The variations of all the temperature values were approximately same irrespective of the catalyst materials utilized in the fuel cell system [22, 24].

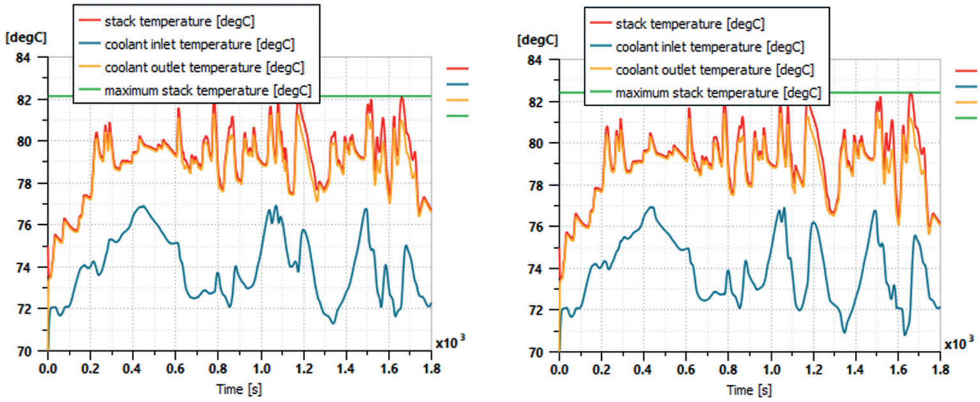

(a) For platinum catalyst material (b) For Fe-N_2-C catalyst material

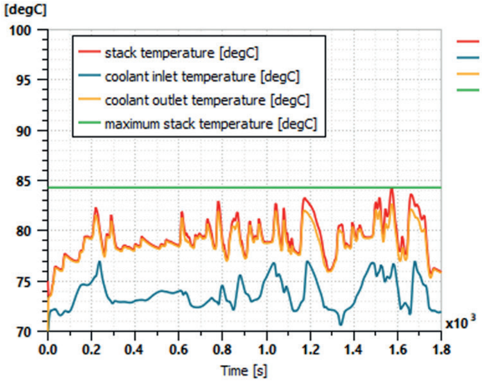

(c) For Ag-alloy catalyst material

Fig. 12. Variation of actual stack temperature, coolant inlet and outlet temperatures and maximum acceptable stack temperature during 1800 seconds of time duration

3.3.4. Variation of Water Content in the Membrane and Proton Area Resistance

Figure 13 shows the variation of water content in the membrane and proton area resistance over a period of driving cycle. From the graphical variations, it is observed that the water content in the membrane decreases as the membrane area resistance increases for all the catalyst materials used in the fuel cell system. Up to 800 seconds, the water content in the membrane drops sharply with the sharp rise in resistance from the proton area. Later, the proton resistance increases with more fluctuations whereas the water content in the member slightly reduces with minor fluctuations. In general, less water content in the member results in lower ion mobility which leads to higher membrane resistance. For Ag-alloy catalyst material, the membrane resistance is slightly higher when compare with platinum and Fe-N_2-C catalyst materials [24].

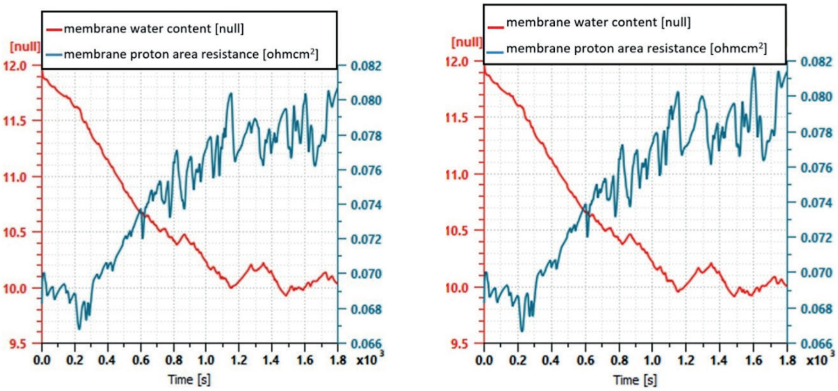

(a) For platinum catalyst material

(b) For Fe-N_2-C catalyst material

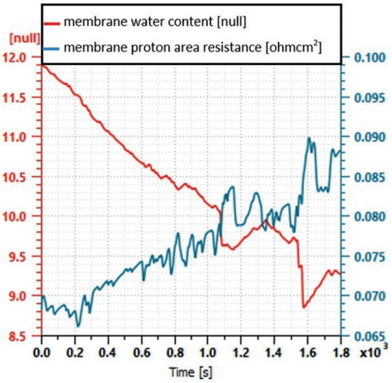

(c) For Ag-alloy catalyst material

Fig. 13. Variation of water content in the membrane and proton area resistance during 1800 seconds of time duration

3.4. Performance Characteristics at Cathode Side

From the performance characteristics of the FCS at cathode side simulation results, the variation of actual air mass flow into FCS versus air mass flow demand, the variations of compressor efficiency, compressor pressure ratio and its speed at corrected air mass flow rate were analysed over a period of 1800 seconds during a cycle.

3.4.1. Variations of Actual and Target Air Mass Flow

Figure 14 shows the variation of actual air mass flow and air mass flow demand over a period of driving cycle. The air mass flow control system controls the mass flow of air with the help of sensor. The air mass flow rate fluctuates widely up to 30 kW over a time and it overlaps with the target curve of air mass flow. The slight deviations in the actual air mass flow may be due to sensor noise, unstable compressor (high pressure ratio), unaccountable environmental changes etc. Increased compressor pressure ratio may lead to slightly increase in air mass flow rate in case of catalyst material Ag-alloy used [22, 24].

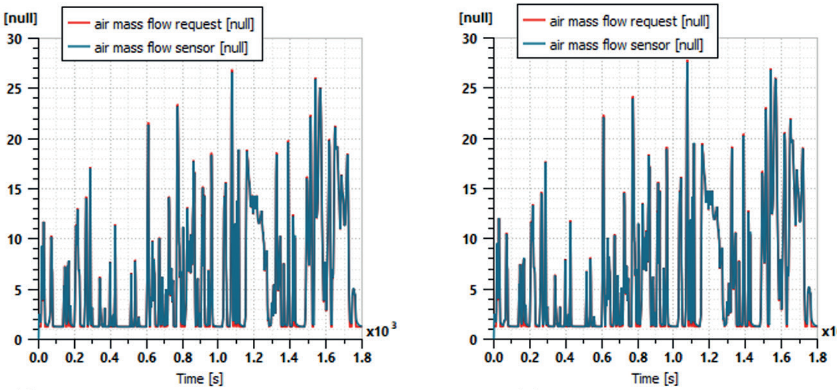

(a) For platinum catalyst material (b) For Fe-N_2-C catalyst material

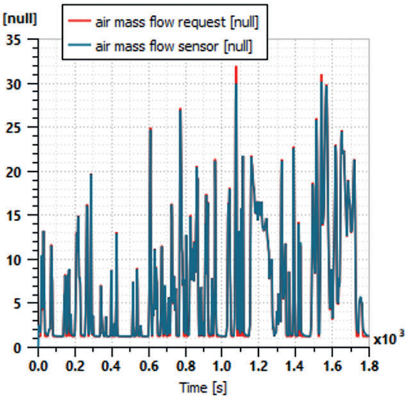

(c) For Ag-alloy catalyst material

Fig. 14. Variation of actual and target air mass flow during 1800 seconds of time duration

3.4.2. Variation of Compressor Efficiency, Corrected Compressor Speed and its Pressure Ratio

Figure 15 shows the variation of compressor efficiency, corrected compressor speed and compressor pressure ratio at different corrected air mass flow rate. The compressor efficiency and the corrected compressor speed show the exactly the same trend for all the catalyst materials used in the fuel cell system. The compressor pressure ratio rises up to 1.6 for the catalyst materials platinum and Fe-N_2-C but it rises up to 1.83 for the catalyst material Ag-alloy. The rise in compressor pressure ratio leads to increase in actual mass flow rate entering the FCS at cathode side [22, 24].

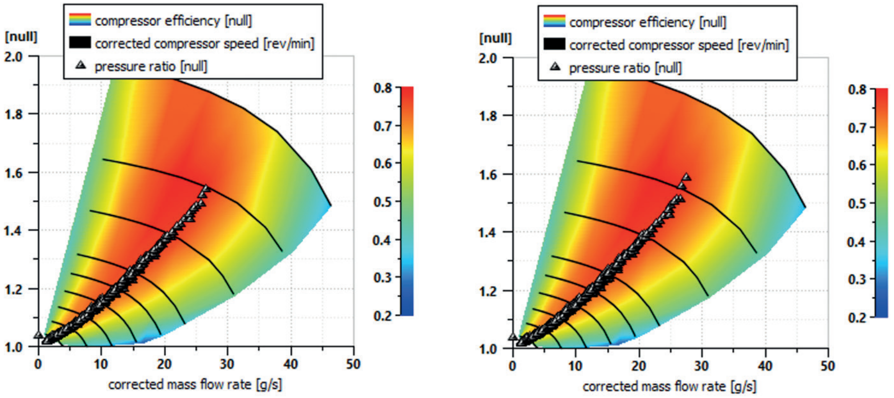

(a) For platinum catalyst material (b) For Fe-N_2-C catalyst material

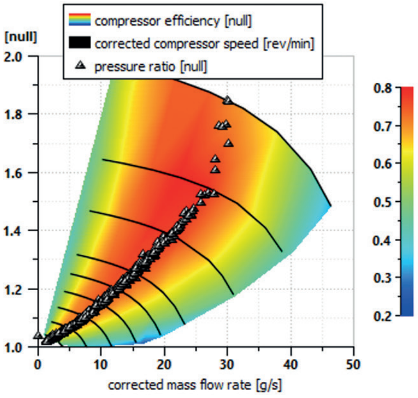

(c) For Ag-alloy catalyst material

Fig. 15. Variation of compressor efficiency, corrected compressor speed and compressor pressure ratio at different corrected mass flow rate of air over 1800 seconds of time duration

3.5. Performance Characteristics at Anode Side

From the performance characteristics of the fuel cell at anode side simulation results, the variation of hydrogen specific consumption and hydrogen purge mass utilization fluctuations were analysed throughout a period of 1800 seconds during a cycle

3.5.1. Variation of Hydrogen Specific Consumption

The efficiency of the fuel cell system is mainly depending on the amount of hydrogen used. Figure 16 shows the variation of hydrogen mass consumed by the fuel cell system over a period of driving cycle. At the time of start-up, the fuel cell system integrated vehicle consumes very high mass of hydrogen above 20 g/km and later the hydrogen consumption rapidly reduces to 9 g/km. Once the system runs (or) vehicle moves, the hydrogen mass consumption slightly fluctuates between 6 g/km to 9 g/km. After reaching steady state operation of fuel cell system, the hydrogen mass consumption fluctuates with minimal range between 7 g/km to 8 g/km. The trend of hydrogen mass consumption is almost same for all the catalyst materials used in the fuel cell system [22].

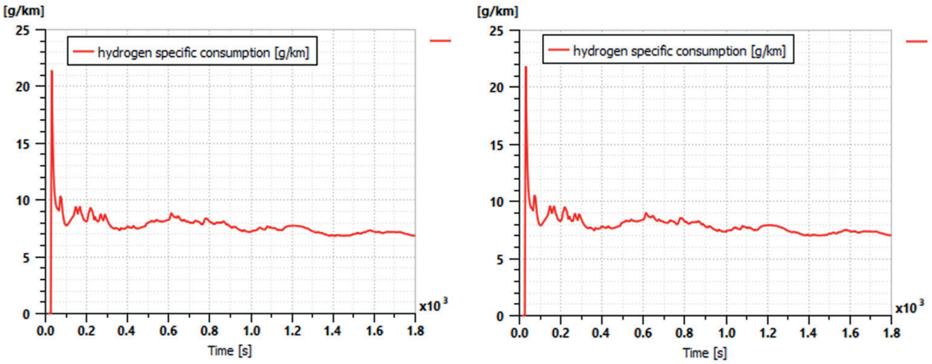

(a) For platinum catalyst material (b) For Fe-N_2-C catalyst material

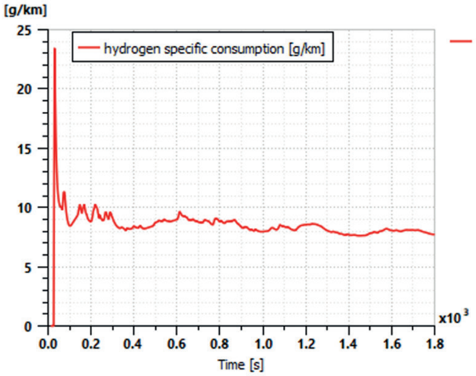

(c) For Ag-alloy catalyst material

Fig. 16. Variation of hydrogen specific consumption over 1800 seconds of time duration

3.5.2. Variation of Hydrogen Purge Mass

To remove water (or) unwanted inert gases and avoid drop in performance of the fuel cell system, the induction of hydrogen purge mass is essential at the anode side of the stack. Figure 17 shows the variation of hydrogen purge mass percentage with respect to time over a driving cycle. At the time of start of the fuel cell system (or) vehicle, there is no induction of hydrogen purge mass due to no accumulation of water (or) unwanted inert gases inside the FCS. In between 200 seconds to 1000 seconds in a driving cycle, these is a sharp rise in hydrogen purge mass up to 5% and later the purge mass varies like a step rise up to 8%. During step rise purge, the system removes the presence of water and inert gases to avoid drop in performance of the FCS. After 1000 seconds, the purge concentration slowly reduces and it fluctuates between 5% to 6% where the system requires less purge due the presence of less concentration of impurities present in the FCS at anode side [24]. The trend of hydrogen purge mass utilization is almost same in all different catalyst materials used.

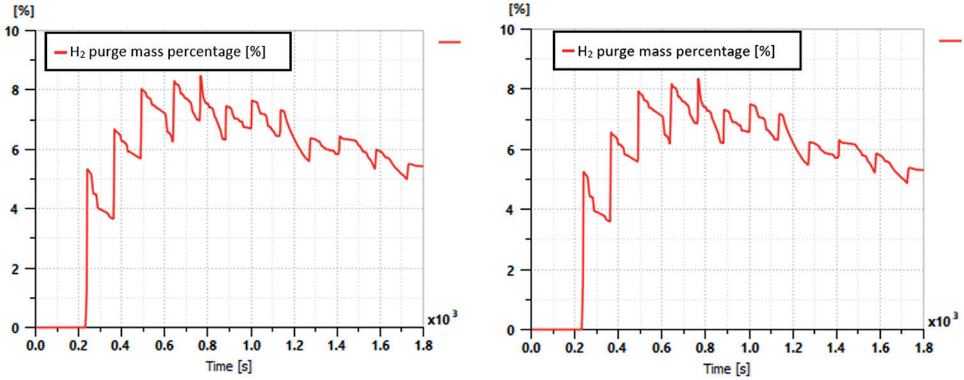

(a) For platinum catalyst material (b) For Fe-N_2-C catalyst material

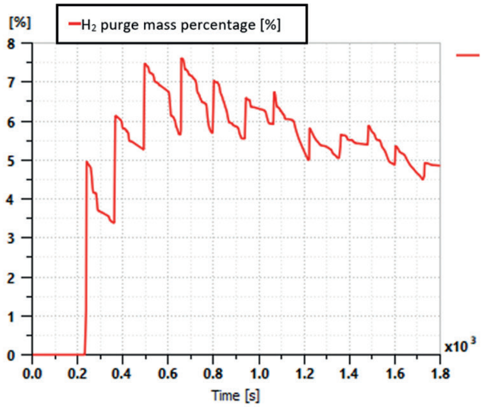

(c) For Ag-alloy catalyst material

Fig. 17. Variation of hydrogen purge mass percentage over 1800 seconds of time duration

3.6. Power Distribution Characteristics

From the power/energy distribution characteristics simulation results, the variations/contributions of hydrogen fuel energy conversion into stack power to propel the vehicle, the part of hydrogen fuel energy converted into electrical energy utilized to operate auxiliary components such as compressor, cooling fan and coolant pump, hydrogen purge energy loss and part of hydrogen fuel energy converted into heat were analysed over a period of 1800 seconds during a cycle.

3.6.1. Variation of Electrical Energy Distribution across Auxiliary Components in Fuel Cell System

Figure 18 shows the electrical energy distribution across the auxiliary components in a fuel cell system. Among the auxiliary components (compressor, radiator fan and coolant pump) in the fuel cell system, compressor drags more energy than other components. The platinum catalyst material used fuel cell system consumed more electrical energy to run the compressor for the supply of air at cathode side of the FCS and it slightly reduces for Fe-N$_2$-C and Ag-alloy catalyst material fuel cell systems [9, 24]. The radiator fan and coolant pump electrical energy demand increases for the catalyst materials platinum, Fe-N$_2$-C and Ag-alloy respectively at 7.2% and 1.0%, 7.9% and 1.3%, and 10.8% and 1.7%.

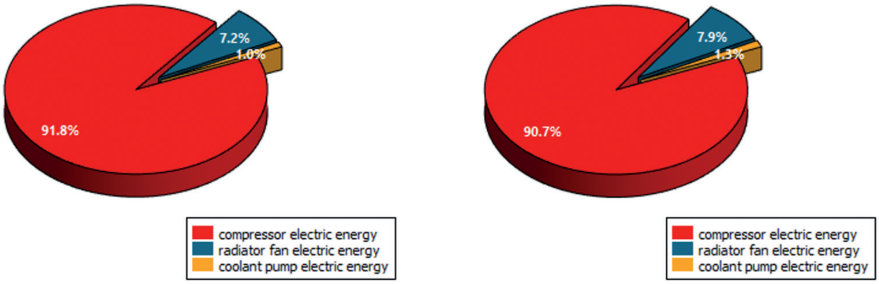

(a) For platinum catalyst material (b) For Fe-N$_2$-C catalyst material

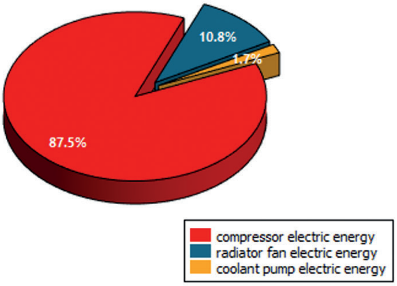

(c) For Ag-alloy catalyst material

Fig. 18. Electrical energy distribution across compressor, radiator fan and coolant pump over 1800 seconds of time duration

3.6.2. Variation of Hydrogen Conversion Energy Distribution

Figure 19 shows the variation of hydrogen conversion energy distribution in a fuel cell system. The maximum mass of hydrogen intake at anode side of the FCS was converted into to stack power used to propel the vehicle. The stack power is comparatively high for the catalyst material platinum and low for Ag-alloy catalyst material. The percentage of hydrogen energy converted into electrical energy known as balance of plant (BoP) was distributed to the auxiliary components in the fuel cell system. The BoP energy low for the catalyst material platinum and high for the catalyst material Ag-alloy. The portion of hydrogen mass converted into heat energy with the fuel cell system (or) sub-system known as thermal energy which is high for the catalyst material platinum and low for Ag-alloy catalyst material. The hydrogen purge energy loss was high in case of platinum catalyst material fuel cell system and low for Ag-alloy catalyst material fuel cell system. The direct loss of hydrogen fuel during hydrogen mass purge reduced the system fuel consumption efficiency [22, 24].

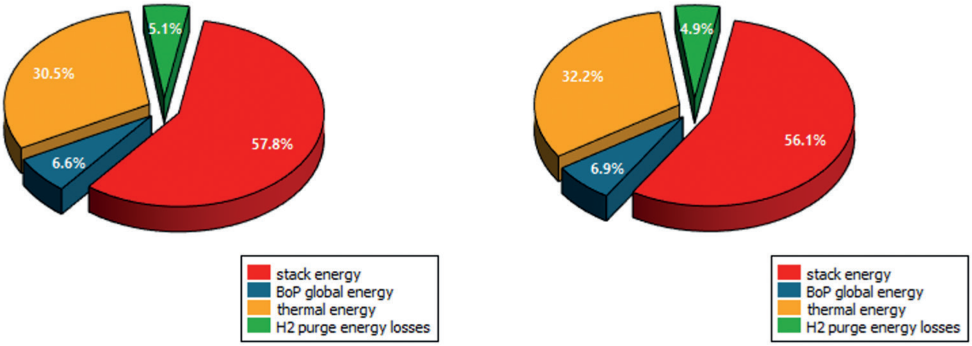

(a) For platinum catalyst material (b) For Fe-N_2-C catalyst material

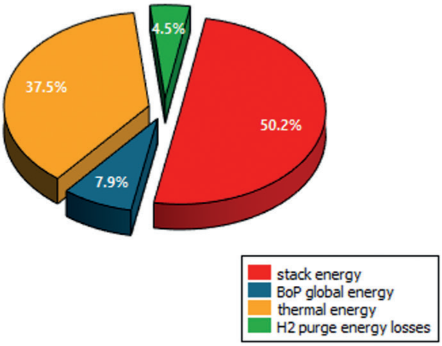

(c) For Ag-alloy catalyst material

Fig. 19. Variation of hydrogen conversion energy distribution in a fuel cell over 1800 seconds of time duration

4. Conclusions

AMESim simulation tool was used to analyse the overall performance of the PEM fuel cell system integrated in a vehicle with platinum, Fe–N_2–C and Ag–alloy catalyst materials for better oxygen reduction reaction under dynamics conditions using adaptive Jacobian computation method. From simulation result graphical variations, the performance characteristics of catalyst materials used in fuel cell system were compared towards vehicle performance, powertrain and stack output power, battery state of charge, compressor efficiency with air mass flow rate, hydrogen fuel efficiency and energy distribution. Fe–N_2–C catalyst material shows relatively the same overall performance like platinum but slightly higher than Ag–alloy catalyst used in the fuel cell system. Few major results were summarized below:

- For all the catalyst materials used for PEM fuel cells, the vehicle travel ranges start fluctuating from 200 km after sudden rise from zero. Later it fluctuates between 600 km to 760 km for platinum and Fe–N_2–C catalyst materials, and between 500 km to 660 km for Ag–alloy catalyst material.
- The maximum compressor pressure ratio shown 1.6 for platinum and Fe–N_2–C catalyst materials whereas for Ag–alloy catalyst material 1.83.
- The cell voltage output range varies from 0.7 V to 0.93 V for the for platinum and Fe–N_2–C catalyst materials but 0.65 V to 0.83 V for Ag–alloy catalyst material.
- The SoC of the battery varies between 70% to 100% for the catalyst materials platinum and Fe–N_2–C catalyst materials but it slightly falls below 70% for Ag–alloy catalyst material.
- The fluctuations trend of motor mechanical power for platinum and Fe–N_2–C catalyst materials shown same whereas Ag–alloy catalyst material shows more deceleration fluctuations between 700 seconds to 1200 seconds during a driving cycle.
- For the same stack power fluctuations among all catalyst materials tested, both platinum and Fe–N_2–C catalyst materials shown maximum heat generation of 20 kW whereas Ag–alloy catalyst material shows the maximum heat generation of 28 kW.
- The stack energy developed was nearly same for platinum and Fe–N_2–C catalyst materials and it comparatively less for Ag–alloy catalyst material.

Also, the price of platinum is much expensive than Fe–N_2–C catalyst material which makes the fuel cell system costlier. From cost benefit point as well as simulation performance results, Fe–N2–C catalyst material proves best suited one to replace costlier platinum catalyst.

4.1. Future Study

The research study can be continued on finding other cheapest catalytic materials for better oxygen reduction reaction with further improved performance of PEM fuel cell.

5. Acknowledgement

We authors thank the management of Chennai Institute of Technology for providing software simulation tool and infrastructural facility to work on this research activity inside the campus.

6. Nomenclature

ORR	Oxygen Reduction Reaction
SoC	State of Charge
PEM	Proton Exchange Membrane
PTFE	Polytetraflourethylene
MEA	Membrane Exchange Assembly
BoP	Balance of Plant
RH	Relative Humidity
FCC	Face Centred Cubic
FCS	Fuel Cell Stack
GDL	Gas Diffusion Layer

7. References

[1] Małek A, Karowiec R, Jóźwik K. A review of technologies in the area of production, storage and use of hydrogen in the automotive industry. The Archives of Automotive Engineering – Archiwum Motoryzacji. 2023;102(4):41–67. https://doi.org/10.14669/AM/177038.

[2] Müller-Hülstede J, Uhlig LM, Schmies H, Schonvogel D, Meyer Q, Nie Y, et al. Towards the Reduction of Pt Loading in High Temperature Proton Exchange Membrane Fuel Cells – Effect of Fe-N-C in Pt-Alloy Cathodes. ChemSusChem. 2023;16(5):e202202046. https://doi.org/10.1002/cssc.202202046.

[3] Mo S, Du L, Huang Z, Chen J, Zhou Y, Wu P, et al. Recent Advances on PEM Fuel Cells: From Key Materials to Membrane Electrode Assembly. Electrochemical energy reviews. 2023;6(1):28. https://doi.org/10.1007/s41918-023-00190-w.

[4] Zierdt T, Müller-Hülstede J, Schmies H, Schonvogel D, Wagner P, Friedrich KA. Effect of Polytetrafluorethylene Content in Fe-N-C-Based Catalyst Layers of Gas Diffusion Electrodes for HT-PEM Fuel Cell Applications. ChemElectroChem. 2024;11(5):e202300583. https://doi.org/10.1002/celc.202300583.

[5] Dafalla AM, Wei L, Habte B, Guo J, Jiang F. Membrane Electrode Assembly Degradation Modeling of Proton Exchange Membrane Fuel Cells: A Review. Energies. 2022;15(23):9247. https://doi.org/10.3390/en15239247.

[6] Müller-Hülstede J, Schmies H, Schonvogel D, Meyer Q, Nie Y, Zhao C, et al. What determines the stability of Fe-N-C catalysts in HT-PEMFCs? International journal of hydrogen energy. 2024;50:921–930. https://doi.org/10.1016/j.ijhydene.2023.09.190.

[7] Xiao F, Wang Q, Xu G, Qin X, Hwang I, Sun C, et al. Atomically dispersed Pt and Fe sites and Pt-Fe nanoparticles for durable proton exchange membrane fuel cells. Nature Catalysis. 2022;5:503–512. https://doi.org/10.1038/s41929-022-00796-1.

[8] Mechler AK, Sahraie NR, Armel V, Zitolo A, Sougrati M, Schwämmlein JN, et al. Stabilization of Iron-Based Fuel Cell Catalysts by Non-Catalytic Platinum. Journal of the Electrochemical Society. 2018;165(13):F1084–F1091. https://doi.org/10.1149/2.0721813jes.

[9] Shen H, Thomas T, Rasaki SA, Saad A, Hu C, Wang J, et al. Oxygen Reduction Reactions of Fe-N-C Catalysts: Current Status and the Way Forward. Electrochemical energy reviews. 2019;2(2):252–276. https://doi.org/10.1007/s41918-019-00030-w.

[10] Asset T, Atanassov P. Iron-Nitrogen-Carbon Catalysts for Proton Exchange Membrane Fuel Cells. Joule. 2020;4(1):33–44. https://doi.org/10.1016/j.joule.2019.12.002.

[11] Maniatis I, Charalampopoulos G, Paloukis F, Daletou MK. Optimizing Fe-N-C Electrocatalysts for PEMFCs: Influence of Constituents and Pyrolysis on Properties and Performance. Catalysts. 2024;14(11):780. https://doi.org/10.3390/catal14110780.

[12] Buschermöhle J, MüllerHülstede J, Schmies H, Schonvogel D, Zierdt T, Lucka R, et al. Fe–Sn–N–C Catalysts: Advancing Oxygen Reduction Reaction Performance. ACS Catalysis. 2025;15(6):4477–4488. https://doi.org/10.1021/acscatal.4c06338.

[13] Kiciński W, Dyjak S, Gratzke M, Tokarz W, Błachowski A. Platinum group metal-free Fe-N-C catalysts for PEM fuel cells derived from nitrogen and sulfur doped synthetic polymers. Fuel. 2022;328:125323. https://doi.org/10.1016/j.fuel.2022.125323.

[14] Sun P, Qiao K, Li D, Liu X, Liu H, Yang L, Xu H, et al. Designing oxygen-doped Fe-N-C oxygen reduction catalysts for proton- and anion-exchange membrane fuel cells. Chem Catalysis. 2022;2(10):2750–2763. https://doi.org/10.1016/j.checat.2022.09.009.

[15] Ma Q, Jin H, Zhu J, Li Z, Xu H, Liu B, et al. Stabilizing Fe–N–C Catalysts as Model for Oxygen Reduction Reaction. Advanced science. 2021;8(23):2102209. https://doi.org/10.1002/advs.202102209.

[16] Malko D, Kucernak A, Lopes T. Performance of Fe-N/C Oxygen Reduction Electrocatalysts toward NO2-, NO, and NH2OH Electroreduction: From Fundamental Insights into the Active Center to a New Method for Environmental Nitrite Destruction. Journal of the American Chemical Society. 2016;138(49):16056–16068. https://doi.org/10.1021/jacs.6b09622.

[17] Qaseem A, Chen F, Wu X, Johnston R. Pt-free silver nanoalloy electrocatalysts for oxygen reduction reaction in alkaline media. Catalysis Science and Technology. 2016;6(10):3317–3340. https://doi.org/10.1039/c5cy02270c.

[18] Linge JM, Erikson H, Merisalu M, Sammelselg V, Tammeveski K. Oxygen reduction on silver catalysts electrodeposited on various nanocarbon supports. SN applied sciences. 2021;3(2). https://doi.org/10.1007/s42452-021-04289-x.

[19] Mondal S, Deshpande S, De SK, Ghosh T, Kharwar Patra S, Karmakar B, et al. Dynamic Strain-Engineered Au-Ag Alloy Nano-Seed Network for Enhanced Electrochemical Oxygen Reduction and High-Performance Alkaline Membrane H2 Air Fuel Cells. Small. 2025. https://doi.org/10.1002/smll.202500555.

[20] BeltránGastélum M, Portillo-Fuentes SG, Flores-Hernández JR, Salazar-Gastélum MI, Trujillo-Navarrete B, Romero-Castañón T, et al. Ag-Cu Nanoparticles as Cathodic Catalysts for an Anion Exchange Membrane Fuel Cell. Catalysts. 2023;13(7):1050. https://doi.org/10.3390/catal13071050.

[21] Farinha J, Silva LM, Matlock J, Afonso F, Suleman A. Hydrogen fuel cell integration and testing in a hybrid-electric propulsion rig. International journal of hydrogen energy. 2023;48(97):38473–38483. https://doi.org/10.1016/j.ijhydene.2023.06.090.

[22] Jiang X, Tao Y, Tang C, Zhao H, Li W. Simulation of Fuel Cell Power Generation System Based on AMESim. IOP conference series Earth and Environmental Science. 2021;770(1):012006. https://doi.org/10.1088/1755-1315/770/1/012006.

[23] Ahmed S, Beauger C, Zada A, Iqbal W, Ahmed N Anwar, MT, Hassan M. Recent advancements in designing high-performance proton exchange membrane fuel cells: A comprehensive review. Applied Energy. 2025;390:125753. https://doi.org/10.1016/j.apenergy.2025.125753.

[24] Ren W, Shen J, Li X, Du C. A Review of Fuel Cell System Technology: From Fuel Cell Stack to System

Integration. International Journal of Automotive Manufacturing and Materials. 2022;1(1):5. https://doi.org/10.53941/ijamm0101005.

[25] Salim R, Noura H, Fardoun A. The Use of LMS AMESim in the Fault Diagnosis of a Commercial PEM Fuel Cell System. Advances in Science, Technology and Engineering Systems Journal. 2018;3(1):297–309. https://doi.org/10.25046/aj030136.